PHYSICS

Quantum-enhanced multiparameter sensing in a single mode

Christophe H. Valahu[1,2,3]*, Matthew P. Stafford[4,5], Zixin Huang[6,7]†, Vassili G. Matsos[1,2], Maverick J. Millican[1,2], Teerawat Chalermpusitarak[1], Nicolas C. Menicucci[8], Joshua Combes[9], Ben Q. Baragiola[8], Ting Rei Tan[1,2,3]*

Precise measurements underpin scientific and technological advancements. Quantum mechanics provides an avenue to enhance precision, but it comes with a restriction: Incompatible observables, such as position and momentum, cannot be simultaneously measured to arbitrary accuracy as decreed by Heisenberg's uncertainty principle. This restriction can be bypassed by instead measuring commuting modular observables, which are counterparts to the naturally incompatible observables. Here, we measure modular observables to estimate small changes in position and momentum with a single-mode multiparameter sensor. We deterministically prepare grid states in the mechanical motion of a trapped ion and demonstrate uncertainties in position and momentum below the standard quantum limit (SQL). Further, we examine another pair of incompatible observables—number and phase. We prepare a different resource—number-phase states—and demonstrate a metrological gain over the SQL. These results introduce previously unidentified measurement capabilities unavailable to classical systems and mark a substantial step in quantum metrology.

INTRODUCTION

Advances in metrology have historically led to breakthroughs in scientific understanding. Galileo's telescope led to the rejection of the geocentric model, while Young's double-slit experiment established the wave properties of light. More recently, gravitational wave detection (*1*, *2*)—a feat of engineering in precision interferometry—has ushered in a new era of astrophysical discoveries. Precision metrology also leads to transformative technologies, such as the global positioning system which harnesses the accuracy of atomic clocks.

The precision of measurements is ultimately limited by quantum mechanical noise, and this limit becomes ever more salient as capabilities improve. The standard quantum limit (SQL) applies when measurements use only classical resources and methods. Surpassing this limit by using quantum resources or measurement strategies is known as quantum metrology (*3*), and it promises to revolutionise precision measurements beyond the capability of conventional sensors. For example, the Laser Interferometer Gravitational-Wave Observatory uses nonclassical light to reduce the measurement uncertainty below the SQL (*4*). Quantum enhancements to sensing have also been demonstrated in atomic clocks (*5*), biological imaging (*6*, *7*), and the search for dark matter (*8*).

When measuring two or more observables that are incompatible, quantum mechanics imposes trade-offs on their uncertainties. This is exemplified by Heisenberg's uncertainty principle: One cannot simultaneously reduce the measurement uncertainty of position and momentum using a probe composed of a single bosonic mode (*9*, *10*). In this context, a mode refers to a single, independent degree of freedom described by observables obeying the canonical commutation relations, typically expressed for bosonic modes in terms of creation and annihilation operators, $\left[\hat{a}, \hat{a}^{\dagger}\right] = 1$. The limit imposed by Heisenberg's uncertainty principle is typically circumvented by using multiple entangled modes, the simplest case being a two-mode squeezed state (*11*–*16*), where enhancements beyond the SQL have been demonstrated at the cost of additional quantum resources (*17*–*19*).

Alternatively, a single mode can simultaneously reduce the uncertainties of two parameters corresponding to incompatible observables with a different trade-off: increased sensitivities at the cost of restrictions on parameter ranges. The reduction in range is unimportant when the parameters are sufficiently small. The key idea is to measure modular variables that are made to commute, circumventing the usual constraint of naturally noncommuting observables imposed by the uncertainty principle (*20*–*24*). This measurement strategy has been theoretically explored for the simultaneous estimations of position and momentum using grid states—a subclass of the Gottesman-Kitaev-Preskill states (*21*) that have been investigated in the context of quantum error correction (*25*–*30*). Ideal grid states allow backaction-evading measurements when sequentially measuring modular position and momentum that commute. Beyond position and momentum, there exist many pairs of noncommuting variables of metrological interest, but simultaneous estimations of them have remained relatively unexplored in the literature.

Here, we demonstrate the simultaneous reduction in uncertainty of two parameters associated with incompatible observables by measuring their modular counterparts. Our experiment uses a single probe made up of a trapped ion's vibrational mode. Our work

[1]School of Physics, University of Sydney, NSW 2006, Australia. [2]ARC Centre of Excellence for Engineered Quantum Systems, University of Sydney, NSW 2006, Australia. [3]Sydney Nano Institute, University of Sydney, NSW 2006, Australia. [4]Quantum Engineering Technology Labs, H. H. Wills Physics Laboratory and Department of Electrical Engineering, University of Bristol, Bristol, UK. [5]Quantum Engineering Centre for Doctoral Training, University of Bristol, Bristol, UK. [6]School of Mathematical and Physical Sciences, Macquarie University, NSW 2109, Australia. [7]Centre for Quantum Software and Information, Faculty of Engineering and Information Technology, University of Technology Sydney, NSW 2007, Australia. [8]Centre for Quantum Computation and Communication Technology, School of Science, RMIT University, VIC 3000, Australia. [9]University of Melbourne, VIC 3052, Australia.
*Corresponding author. Email: christophe.valahu@sydney.edu.au (C.H.V.); tingrei.tan@sydney.edu.au (T.R.T.)
†Present address: School of Science, College of STEM, RMIT University, Melbourne, Australia.

draws on concepts and techniques developed for error-corrected quantum information processing—such as logical qubit encodings, stabilizer syndrome extractions, and optimal control—and adapts them for metrology. We first consider multiparameter displacement sensing using grid states and demonstrate a clear metrological gain over the SQL. We then perform a quantum phase estimation (QPE) algorithm with Bayesian inference and find that an adaptive strategy performs better than a nonadaptive strategy. Furthermore, we investigate simultaneous estimations of number and phase, which do not commute. This is achieved by using number-phase (NP) states (*31*), which are the polar counterparts of grid states that were only theoretically explored because of no previously known experimental scheme to prepare the states. We develop the necessary quantum control for operations with these states and demonstrate a metrological gain over the simultaneous SQL of number and phase. In so doing, we introduce—and experimentally realize—a resource for quantum sensing on which we plan further theoretical and experimental investigations.

RESULTS

We first consider the simultaneous estimation of position, $\hat{x}$, and momentum, $\hat{p}$, whose uncertainties follow the uncertainty principle, $\Delta x \Delta p \geq \hbar/2$ (see Fig. 1A) (*9*, *10*). This limit is circumvented by instead measuring their modular counterpart, $\hat{x}_{[2\pi/l_x]}$ and $\hat{p}_{[2\pi/l_p]}$, where $\hat{q}_{[m]} = \hat{q} \mod m$ (see Fig. 1B). Modular position and momentum are observables of $\hat{x}$ and $\hat{p}$ up to a modulus $2\pi/l_x$ and $2\pi/l_p$, respectively. By setting $l_{x,p} = l_s = \sqrt{2\pi}$, modular position and momentum commute, giving the uncertainty relation $\Delta\hat{x}_{[2\pi/l_s]}\Delta\hat{p}_{[2\pi/l_s]} \geq 0$. This commutation relation was investigated by a signaling-in-time experiment and a violation of the Leggett-Garg inequality (*24*).

We exploit the compatibility of these observables to simultaneously sense small displacements of position and momentum below the SQL. To do so, we use grid states, $|\#\rangle$, which are simultaneous eigenstates of the shift operators $\hat{S}_x = e^{-il_s\hat{x}_{[2\pi/l_s]}} = e^{-il_s\hat{x}}$ and $\hat{S}_p = e^{-il_s\hat{p}_{[2\pi/l_s]}} = e^{-il_s\hat{p}}$. Grid states are periodic in $\hat{x}$ and $\hat{p}$ and have peaks in phase space located on points of a square lattice of size l_s (see Fig. 1C). The ideal grid states are unphysical as they have infinite energy. We instead consider finite-energy approximations to these states, $|\,\#\,\rangle$, given by a weighted superposition of squeezed states parameterised by Δ, which serves as a measure of quality. Ideal grid states are recovered in the limit $\Delta \to 0$. Physical grid states are used for multiparameter sensing in the following way: After an unknown displacement, $|\,\widetilde{\#}_\epsilon\,\rangle = e^{i\epsilon_p\hat{x}}e^{-i\epsilon_x\hat{p}}\,|\,\widetilde{\#}\,\rangle$ with displacement parameters $\epsilon_x, \epsilon_p \in \mathbb{R}$, one can estimate $\epsilon_x \mod \sqrt{2\pi}$ and $\epsilon_p \mod \sqrt{2\pi}$ by estimating the eigenvalues of $\hat{S}_x$ and $\hat{S}_p$. Applying these operators gives $\hat{S}_x\,|\,\tilde{\#}_\epsilon\rangle \approx e^{-i\sqrt{2\pi}\epsilon_x}\,|\,\tilde{\#}_\epsilon\rangle$ and $\hat{S}_p\,|\,\tilde{\#}_\epsilon\rangle \approx e^{-i\sqrt{2\pi}\epsilon_p}\,|\,\tilde{\#}_\epsilon\rangle$, and the displacement parameters are then retrieved by estimating the phases, $\sqrt{2\pi}\epsilon_x$ and $\sqrt{2\pi}\epsilon_p$, imprinted on the sensing state via a QPE algorithm. These modular measurements give unambiguous estimations of position and momentum if it is known a priori that the displacement parameters are smaller than $\sqrt{2\pi}$. In systems where this is not known, the above measurement protocol estimates the remainder of the modulus, but the integer part remains unknown.

The circuit to perform multiparameter sensing is depicted in Fig. 1E. After preparing the sensing state and undergoing an unknown displacement, a sequence of QPE subroutines (blue boxes) is applied in

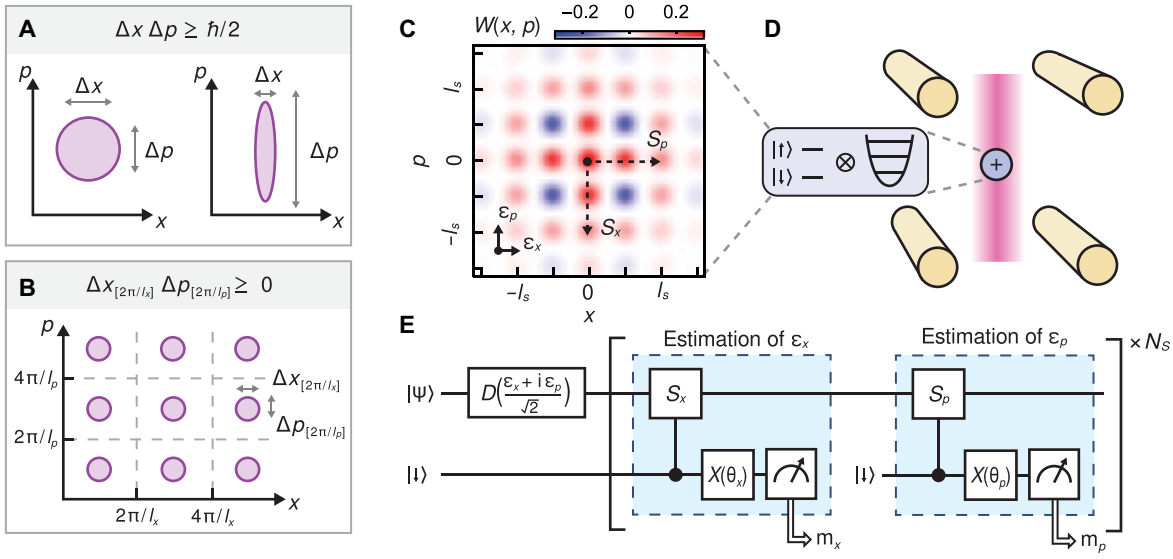

Fig. 1. Multiparameter quantum enhanced sensing. (**A**) The uncertainty in simultaneous position-momentum measurements is bounded by the canonical commutation relation. (**B**) Their modular counterparts can instead be made to commute, allowing for estimation of $\hat{x}_{[2\pi/l_x]}$ and $\hat{p}_{[2\pi/l_p]}$ with uncertainties simultaneously below the SQL, where $l_s = l_x = l_p = \sqrt{2\pi}$ are the modulus lengths. (**C**) The eigenstates of modular position-momentum are grid states (shown is the Wigner function), which can sense displacements in position by ϵ_x and displacements in momentum by ϵ_p by measuring commuting operators $\hat{S}_x$ and $\hat{S}_p$. (**D**) Physical grid states are prepared in the bosonic mode of a trapped ion. An ancilla qubit encoded in the electronic ground state of the ion couples to the bosonic mode via a laser interaction (pink beam), allowing for measurement of position and momentum observables. (**E**) A QPE circuit is used for multiparameter estimation of ϵ_x and ϵ_p. After preparing the sensing state and undergoing an unknown displacement, multiple rounds of a QPE subroutine (blue box) are applied, where each round applies conditional $\hat{S}_x$ or $\hat{S}_p$, which gives one bit of phase estimation, m_x or m_p. Since $\hat{S}_x$ and $\hat{S}_p$ commute, they can be applied alternately N_s times, ideally performing many rounds of backaction-evading measurements.

an alternating fashion. Each subroutine first applies a conditional momentum or position operator, $C\hat{S}_x = e^{-il_s\hat{\sigma}_x\hat{x}/2}$ or $C\hat{S}_p = e^{-il_s\hat{\sigma}_x\hat{p}/2}$, which maps information from the bosonic mode to an ancillary two-level system. A measurement of the ancilla then gives a binary measurement outcome $m_x \in \{0,1\}$ or $m_p \in \{0,1\}$, with probability distributions

$$P_x(m_x|\epsilon_x,\theta_x) = \frac{1}{2}\left[1+(-1)^{m_x}\eta_x\cos(\epsilon_x l_s+\theta_x)\right] \quad (1)$$

$$P_p(m_p|\epsilon_p,\theta_p) = \frac{1}{2}\left[1+(-1)^{m_p}\eta_p\cos(\epsilon_p l_s+\theta_p)\right] \quad (2)$$

The visibility parameters $\eta_x = \left\langle \hat{S}_x + \hat{S}_x^\dagger \right\rangle/2 = \mathrm{Re}\left[\chi\left(i\sqrt{\pi}\right)\right]$ and $\eta_p = \left\langle \hat{S}_p + \hat{S}_p^\dagger \right\rangle/2 = \mathrm{Re}\left[\chi\left(-\sqrt{\pi}\right)\right]$ correspond to values of the characteristic function on the square lattice (see Fig. 2A), where $\chi(\beta) = \left\langle \hat{D}^\dagger(\beta) \right\rangle$ and $\beta \in \mathbb{C}$ is the phase space location where the characteristic function is sampled. The visibility parameters are $\eta_x = \eta_p = 1$ for an ideal grid state with $\Delta = 0$. The phases θ_x and θ_p are controllable and are introduced by an ancilla rotation (see Fig. 1E). The probability distribution P_x and P_p are only dependent on one of the parameters, ϵ_x or ϵ_p, respectively. Therefore, each measurement outcome can be used to independently retrieve ϵ_x or ϵ_p.

Our experiment is performed with a single $^{171}Yb^+$ ion confined in a room temperature macroscopic Paul trap. The sensing states are encoded in the vibrational bosonic mode along a radial direction with a frequency of $\omega_x = 2\pi \times 1.33\,\mathrm{MHz}$. An ancillary qubit is encoded in the "atomic clock" state of the hyperfine ground state with labels $|\downarrow\rangle \equiv |F=0, m_f=0\rangle$ and $|\uparrow\rangle \equiv |F=1, m_f=0\rangle$ and is used to assist in the preparation of sensing states and measurements; see (*32*–*34*) for more details on the experimental system.

The coherent control required to prepare the grid states and measure observables is performed with a laser-driven state-dependent force (SDF) that couples the ancillary qubit and the vibrational mode (see Materials and Methods). An SDF is enacted by stimulated Raman transitions from a pair of orthogonal beams derived from a 355-nm pulsed laser. The Hamiltonian of the SDF in the interaction frame of both the qubit and the vibrational mode is

$$\hat{H}_{\mathrm{SDF}}(t) = \frac{\Omega}{2}\left[\hat{\sigma}_x\cos\phi_s(t) + \hat{\sigma}_y\sin\phi_s(t)\right] \times \left(\hat{a}^\dagger e^{-i\phi_m(t)} + \hat{a}e^{i\phi_m(t)}\right) \quad (3)$$

The interaction strength Ω is controllable by varying the laser power, while the phases $\phi_s(t)$ and $\phi_m(t)$ are tuneable by modulating an acousto-optic modulator (AOM) in the path of one of the Raman beams. The controlled position and momentum operators are obtained by applying $\hat{H}_{\mathrm{SDF}}$ for a duration $t = \sqrt{\pi}/\Omega$. Setting $(\phi_s, \phi_m) = (0,0)$ gives $C\hat{S}_x$, while setting $(\phi_s, \phi_m) = (\pi, \pi/2)$ gives $C\hat{S}_p$.

Here, the circuit of Fig. 1E is implemented as follows. First, the sensing state is prepared by applying $\hat{H}_{\mathrm{SDF}}(t)$ with dynamically modulated phases $\phi_s(t)$ and $\phi_m(t)$. The phase modulation waveforms are numerically optimized to prepare grid states with varying target squeezing parameters; see (*34*) and Materials and Methods. The waveforms are modeled as piecewise constant functions with 30 optimizable segments, and the resulting durations are in the range of 0.3 to 1.5 ms. We also constrain the numerical optimization such that the ancilla returns to the $|\downarrow\rangle$ state after applying the pulse and is disentangled from the motional mode. Second, the sensing states are subjected to a force which displaces the state by $\hat{D}\left[\frac{1}{\sqrt{2}}(\epsilon_x + i\epsilon_p)\right]$. In our experiment, this force is controllably injected by applying a laser-driven interaction, $\hat{H}_{\mathrm{SDF}}$, for a duration $t = \sqrt{2}|\epsilon_x + i\epsilon_p|/\Omega$ with $\phi_s = 0$ and $\phi_m = -\pi/2 - \arg(\epsilon_x + i\epsilon_p)$. The SDF is surrounded by pulses that rotate the ancilla in and out of a $\hat{\sigma}_x$ eigenstate, such that it remains disentangled from the motion after applying $\hat{H}_{\mathrm{SDF}}$. We then perform QPE and retrieve measurement outcomes m_x and m_p by performing ancilla measurements in the $\hat{\sigma}_z$ basis through state-dependent fluorescence. Detections of $|\downarrow\rangle$ and $|\uparrow\rangle$ correspond to measurement outcomes of 0 and 1, respectively. Photons scattered from measurement outcomes of 1 decohere the sensing state due to their recoil energy; hence, the experiment only proceeds if

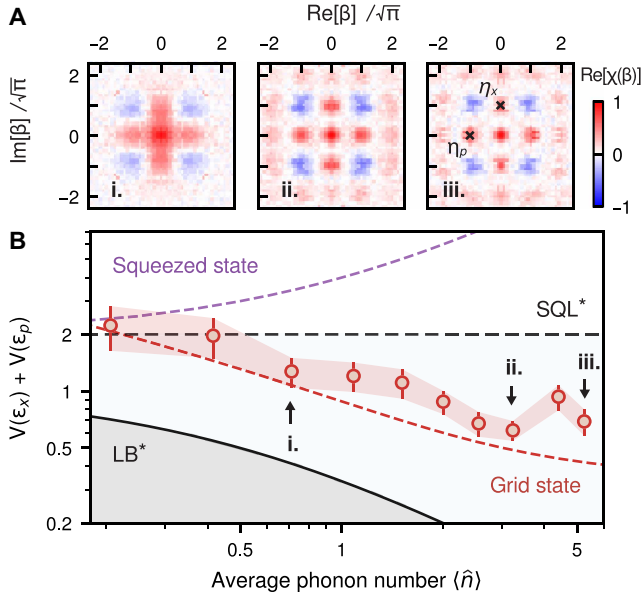

Fig. 2. Metrological gain of grid states for multiparameter displacement sensing. (**A**) Experimentally reconstructed characteristic function of prepared grid states with target parameters Δ of (i) 0.61, (ii) 0.37, and (iii) 0.30. Increasing energy results in increased squeezing along position and momentum. Crosses in (iii) show points of the characteristic function that correspond to values of the visibility parameters $\eta_x = \mathrm{Re}\left[\chi\left(i\sqrt{\pi}\right)\right]$ and $\eta_p = \mathrm{Re}\left[\chi\left(-\sqrt{\pi}\right)\right]$. (**B**) Multiparameter variance, $V(\epsilon_x) + V(\epsilon_p)$, of grid states with increasing average phonon number, $\langle\hat{n}\rangle$. Variances (red circles) are calculated from the classical Fisher information of the experimentally measured probability distributions P_x and P_p. The sensing signal is varied in the range $\{\epsilon_x, \epsilon_p\} \in [0,1.4]$. Error bars correspond to one SD calculated from quantum projection noise. Red dashed line is the expected multiparameter variance of the target grid states. The SQL* corresponds to the multiparameter variance of a coherent state from heterodyne measurement (see the Supplementary Materials). The simultaneous lower bound (LB*) plots the minimum uncertainty from the quantum Fisher information, $1/(2\langle\hat{n}\rangle+1)$ (*17*, *23*). Purple dashed line corresponds to the multiparameter variance from heterodyne detection, with a single-mode squeezed state squeezed in one quadrature and antisqueezed in the other. Heterodyne detection is equivalent to double homodyne detection: The state is split by a 50:50 beam splitter, with position measured on one output and momentum on the other (*67*).

the measurement outcome is 0. Measurement outcomes of 1 are instead obtained by randomly initialising the ancillary qubit in $|\downarrow\rangle$ or $|\uparrow\rangle$ with equal probability at the beginning of a QPE subroutine. We then record an outcome of 0 or 1 if the qubit was initialized in $|\downarrow\rangle$ or $|\uparrow\rangle$, respectively.

In the first experiment, we characterize the metrological gain of the grid states by calculating the multiparameter variance. To this end, we reconstruct the probability distributions of Eqs. 1 and 2 using the QPE circuit of Fig. 1E with varying ϵ_x and ϵ_p. For each pair $\{\epsilon_x, \epsilon_p\}$, we set $\theta_x = \theta_p = 0$ and perform the QPE circuit M times. The probabilities $P_x(m_x|\epsilon_x)$ and $P_p(m_p|\epsilon_p)$ are calculated from the mean of the outcomes m_x and m_p. Repeating this over a range of $\{\epsilon_x, \epsilon_p\}$ gives two-dimensional probability distributions. These are used to compute the 2×2 Fisher information matrix $\mathbf{F}$, which quantifies the amount of information corresponding to $\{\epsilon_x, \epsilon_p\}$ that is contained in the measurement outcomes. From the Fisher information matrix, we compute the 2×2 covariance matrix, $\Sigma = \mathbf{F}^{-1}$. The multiparameter variance is then bounded by minimizing the trace of the covariance matrix over the range $\{\epsilon_x, \epsilon_p\}$, $V(\epsilon_x) + V(\epsilon_p) \geq \min_{\epsilon_x,\epsilon_p} \mathrm{Tr}(\Sigma)$ (*17*). This procedure is repeated for grid states with different average phonon numbers, $\langle \hat{n} \rangle$, with results summarized in Fig. 2. The experiment agrees well with theory, where the uncertainty decreases with $\langle \hat{n} \rangle$. This improvement is corroborated by the reconstructed characteristic functions of the grid states, whose peaks are more squeezed with larger $\langle \hat{n} \rangle$ (Fig. 2A). The lowest variance is obtained at $\langle \hat{n} \rangle = 3.2$ ($\Delta = 0.37$), giving a gain of 5.1(5) dB over the simultaneous SQL (here and throughout, the terminology SQL* is used to refer to the simultaneous SQL for two noncommuting quadrature measurements). We observe that the variance does not further decrease for $\langle \hat{n} \rangle > 3.2$, and we attribute this to dephasing of the motional mode.

In the second experiment, we perform multiparameter displacement sensing with a grid state to find estimates $\{\tilde{\epsilon}_x, \tilde{\epsilon}_p\}$ of a random signal $\{\epsilon_x, \epsilon_p\}$. The estimation procedure uses Bayesian inference as follows (*35*). Starting from a prior distribution for $\{\epsilon_x, \epsilon_p\}$, the QPE circuit of Fig. 1E is performed once with $N_S = 1$ to give two measurement outcomes, m_x and m_p, whose probability distributions follow Eqs. 1 and 2. A posterior distribution is then calculated from both the prior and the new measurement outcomes using Bayes' theorem. We determine $\{\tilde{\epsilon}_x, \tilde{\epsilon}_p\}$ by maximizing the posterior after several measurement iterations where the posterior distribution converges.

The results of this Bayesian QPE are plotted in Fig. 3. We measure the Holevo variance, defined as $V_H(\tilde{\epsilon}_{x,p}) = \left(|\langle e^{il_s\tilde{\epsilon}_{x,p}}\rangle|\right)^{-2} - 1$ (*36*), which we average over many randomly sampled signals $\{\epsilon_x, \epsilon_p\}$ and vary the number of measurement repetitions, M. We first perform nonadaptive QPE, where the phases of the ancilla rotation at the mth iteration are set to $\theta_{x,m} = \theta_{p,m} = \pi m / M$. We observe that $V_H(\tilde{\epsilon}_p)$ (purple circles) is larger than $V_H(\tilde{\epsilon}_x)$ (blue circles), which is due to ϵ_p being measured after ϵ_x and therefore suffers more decoherence. As there are no theoretical restrictions on the ordering of the measurement operations, one could alternate between first measuring ϵ_x or ϵ_p to balance their variances. The total variance (red circles) decreases with M as expected and falls below SQL* at $M = 128$. To further reduce the variance, we perform adaptive QPE where the phases $\theta_{x,m}$ and $\theta_{p,m}$ are optimized in real-time before each mth measurement iteration (*37*, *38*). This protocol maximizes the information gained, and we achieve a combined variance 2.6 (1.1) dB below SQL*. Variances at $M < 128$ obtained from nonadaptive QPE are above SQL* due to small-sample size effects, and the variance is expected to reach the Cramer-Rao bound as M increases (*38*).

In a separate experiment, we investigate the potential of further leveraging backaction evasion by repeatedly measuring $\hat{S}_x$ and $\hat{S}_p$ for N_S times within a single circuit iteration. We derive the joint probability distribution with arbitrary N_S and find that it can be conveniently described by only a few points of the characteristic function lying on the lattice. Moreover, effects from backaction due to finite-energy grid states can be incorporated into the estimation analysis, allowing us to straightforwardly perform the same nonadaptive Bayesian estimation detailed above. With $M = 32$, the combined variance is reduced by 1.4 dB from $N_S = 1$ to $N_S = 2$ (see circuit of Fig. 1E). No discernible improvement in metrological gain is observed for $N_S = 3$, which we attribute primarily to the dephasing of the sensing state, evidenced by independent measurements of the lifetimes of $\hat{S}_x$ and $\hat{S}_p$ (see the Supplementary Materials). The variance could be further reduced by minimizing backactions using finite-energy $C\hat{S}_x$ and $C\hat{S}_p$ operators tailored to the physical grid states (*39*, *40*). Repeating the experiment in Fig. 2 with finite-energy operators gives an improved metrological gain of 6.0(5) dB (see the Supplementary Materials).

Moving beyond position-momentum, we investigate simultaneous multiparameter estimations of number and phase, which adhere to the uncertainty relation $\Delta n \Delta\phi \geq \hbar/2$, where $(\Delta\phi)^2$ is the Holevo

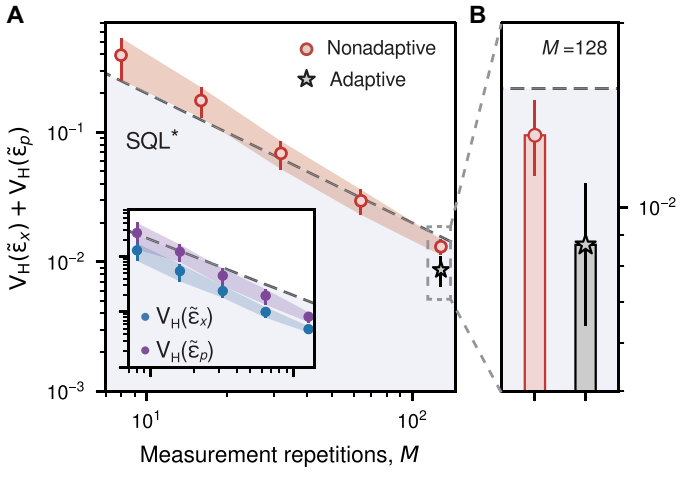

Fig. 3. QPE with grid states. (**A**) The multiparameter variance of a grid state with $\Delta = 0.41$ is measured for increasing measurement repetitions $M \in [8,128]$ with $N_S = 1$ QPE subroutine repetitions. Estimates $(\tilde{\epsilon}_x, \tilde{\epsilon}_p)$ of an unknown displacement $\hat{D}\left[(\epsilon_x + i\epsilon_p)/\sqrt{2}\right]$ are obtained from a QPE algorithm using a nonadaptive routine (red circles), where the control phases $(\theta_{x,p})$ are predetermined before the experiment. Inset plots the individual variances and shares the same x and y axes as the main plot. Dashed line plots SQL*, which is equal to $2/M$. The nonadaptive variance is below SQL* at $M = 128$ measurements. The variance is further reduced by using an adaptive protocol (black star), where the control phases are optimized in real time. (**B**) Zoom-in examination at $M = 128$, where adaptive QPE outperforms both SQL* and the nonadaptive measurement. Error bars correspond to one SD calculated from quantum projection noise.

phase variance (*41*). The corresponding sensing states are referred to as NP states, $|\oplus\rangle$. In analogy to grid states, NP states are simultaneous eigenstates of two shift operators: the number operator, $\hat{S}_n = e^{-il_n\hat{n}}$, which is used to estimate shifts in number, and the phase operator (*31*), $\hat{S}_\phi = \hat{E}^-_{l_\phi}$, which is used to estimate shifts in phase. The former is a rotation, and the latter is a phonon-shift operator defined as $\hat{E}^-_{l_\phi} = \left(\hat{E}^-\right)^{l_\phi}$, where $\hat{E}^- = \sum_{n=0}^{\infty} |n\rangle\langle n+1|$ is the Susskind-Glogower phase operator, which lowers phonon number by one in an unweighted way (independent of the Fock state) (*42*). $\hat{S}_n$ and $\hat{S}_\phi$ commute by setting $l_n = 2\pi/N$ and $l_\phi = N$, where the positive integer N can be freely chosen. The resulting ideal and unnormalized eigenstates, $|\oplus\rangle = \sum_{k=0}^{\infty} |kN\rangle$, are periodic in Fock space with a spacing given by N and have a $2\pi/N$ rotational symmetry in phase space; see Fig. 4 (A and B). NP states can simultaneously sense a continuous rotation and a discrete shift in number: Given an unknown rotation and phonon shift described by $|\oplus_\epsilon\rangle = e^{i\epsilon_\phi\hat{n}}\hat{E}^+_{\epsilon_n}|\oplus\rangle$, the parameters ϵ_n and ϵ_ϕ can be estimated from the eigenvalues of $\hat{S}_n$ and $\hat{S}_\phi$, respectively. Applying the number and phase operators results in $\hat{S}_n|\oplus_\epsilon\rangle = e^{-i\epsilon_n l_n}|\oplus_\epsilon\rangle$ and $\hat{S}_\phi|\oplus_\epsilon\rangle = e^{-i\epsilon_\phi l_\phi}|\oplus_\epsilon\rangle$, allowing one to estimate $\epsilon_n \mod N$ and $\epsilon_\phi \mod 2\pi/N$.

Experiments with NP states follow the general structure shown in Fig. 1E by replacing the sensing states and associated measurement operators. We apply numerically optimized phase-modulated $\hat{H}_{\mathrm{SDF}}$ to create finite-energy NP states, $|\widetilde{\oplus}\rangle$, which are made physical by applying a sinusoidal damping envelope with a finite cutoff to the Fock state probability distribution of idealised NP states . We verify the prepared NP states by reconstructing the characteristic functions and find good agreement with theory; see Fig. 4 (B and C) and the Supplementary Materials for the data.

QPE routines for NP states are analogously performed by first applying a conditional number or phase operator and then measuring the ancilla. The conditional operations are implemented by driving "blue-sideband" (BSB) interactions (details in the Supplementary Materials) described by the Hamiltonian

$$\hat{H}_{\mathrm{b},k} = \frac{\Omega_{\mathrm{b},k}}{2}\hat{\sigma}^+\left(\hat{a}^\dagger\right)^k e^{-i\delta_{\mathrm{b},k}t}e^{-i\phi_{\mathrm{b},k}} + \mathrm{h.c.} \quad (4)$$

where $k = 1$ ($k = 2$) gives the first (second) order interaction. A conditional number operator, $C\hat{S}_n = e^{-il_n\hat{\sigma}_z\hat{n}/2}$, is obtained by setting $\phi_{\mathrm{b},k} = 0$ and $\delta_{\mathrm{b},k} \gg \Omega_{\mathrm{b},k}$, where $\phi_{\mathrm{b},k}$, $\delta_{\mathrm{b},k}$, and $\Omega_{\mathrm{b},k}$ are the phase, detuning, and Rabi rate of the interaction. A weaker second-order interaction with $\Omega_{\mathrm{b},2} \ll \Omega_{\mathrm{b},1}$ is applied to counter-act parasitic interactions from the first-order field that would otherwise introduce errors.

The controlled phase operator, $C\hat{S}_\phi$, is implemented by alternately applying $\hat{H}_{\mathrm{b},1}$ and a qubit rotation (*43*). We set $\hat{H}_{\mathrm{b},2} = 0$ and $\delta_{\mathrm{b},1} = 0$, and $\phi_{\mathrm{b},1}(t)$ is dynamically modulated with a numerically optimized waveform such that applying $\hat{H}_{\mathrm{b},1}$ enacts the transition $|\downarrow, n\rangle \rightarrow |\uparrow, n+1\rangle$ with coupling strength independent of n. Applying a $\hat{\sigma}_x$ π-pulse then returns the qubit to its original state, $|\uparrow, n+1\rangle \rightarrow |\downarrow, n+1\rangle$. A single iteration of BSB-$\hat{\sigma}_x$ sequence gives a Susskind-Glogower phase operator conditioned on the ancilla (*42*): The $|\downarrow\rangle$ state results in an upward shift operator, $|\downarrow\rangle\langle\downarrow|\hat{E}^+$, while the $|\uparrow\rangle$ state results in a downward shift operator, $|\uparrow\rangle\langle\uparrow|\hat{E}^-$. The overall $C\hat{S}_\phi$ operator is then implemented by applying the BSB-$\hat{\sigma}_x$ sequence $l_\phi/2$ times, giving $C\hat{S}_\phi = |\downarrow\rangle\langle\downarrow|\hat{E}^+_{l_\phi/2} + |\uparrow\rangle\langle\uparrow|\hat{E}^-_{l_\phi/2}$. Applying $\hat{E}^-$ to states in $|n=0\rangle$ causes unwanted rotations of the ancilla, which we avoid by using NP states with Fock state populations that are shifted by $\hat{E}^+_{l_\phi/2}$.

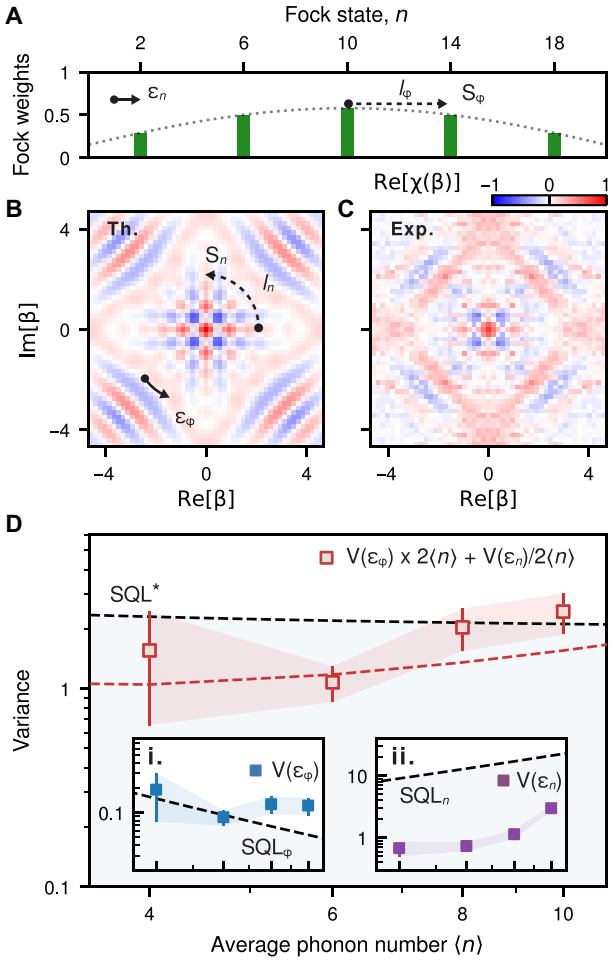

Fig. 4. Metrological gain of NP states for multiparameter number and phase sensing. (**A** and **B**) Theoretical Fock distribution and characteristic function of a NP state with spacing $N = 4$, Fock cutoff $F = 18$, and offset of 2 (lowest occupied Fock state is $|n = 2\rangle$). The energy of this state is constrained by damping the Fock coefficients with a sine envelope (gray dotted line), giving $\langle\hat{n}\rangle = 10$. The NP state has exact rotational phase-space symmetry of $l_n = 2\pi/4$ and approximate translational Fock symmetry of $l_\phi = 4$, making it an exact eigenstate of $\hat{S}_n$ and an approximate eigenstate of $\hat{S}_\phi$. This spacing in phase and number can be used to simultaneously sense small unknown rotations by ϵ_ϕ in phase space and shifts by ϵ_n in Fock space. (**C**) Experimentally reconstructed characteristic function of the above NP state. (**D**) The variances of number and phase are obtained from the classical Fisher information extracted from reconstructed probability distributions. Red dashed line is the expected multiparameter variance of the target NP state. Insets (i and ii) plot the individual variances for number and phase, with $\mathrm{SQL}_n = 2\langle\hat{n}\rangle + 1$ and $\mathrm{SQL}_\phi = \left(2\langle\hat{n}\rangle\right)^{-1} + 3\left(8\langle\hat{n}\rangle^2\right)^{-1}$, which correspond to a coherent state subjected to heterodyne measurements (see the Supplementary Materials). SQL* is the sum of SQL for number and phase after rescaling by $\left(2\langle\hat{n}\rangle\right)^{-1}$ and $2\langle\hat{n}\rangle$, respectively, such that both variances are equal to 1 and $\mathrm{SQL}^* = 2$ at large $\langle n\rangle$. The combined variances (red squares) are the total of $\mathrm{V}(\epsilon_n)$ and $\mathrm{V}(\epsilon_\phi)$ after appropriately rescaling the covariance matrix. Error bars correspond to one SD calculated from quantum projection noise.

The choice of spacing, N, of the target NP state is subject to several tradeoffs. First, the theoretical variances of number and phase scale with N as $\mathrm{V}(\epsilon_n) \propto N^2$ and $\mathrm{V}(\epsilon_\phi) \propto 1/N^2$. Second, increasing N reduces the visibility parameter of the phase operator, $\eta_\phi = \left\langle \hat{E}^-_{l_\phi} \right\rangle$, which quantifies the metrological performance in the QPE algorithm and should ideally be 1. In contrast, the visibility parameter associated with the number operator is independent of N and is $\eta_n = 1$, since NP states are exact eigenstates of $\hat{S}_n$. Third, the choice of N influences the quality of the experimental implementations of number and phase operators. Large N improves the quality of the controlled number operator, as the target phase parametrized by l_n becomes smaller, thereby reducing higher-order terms and enabling shorter pulse duration. However, large N degrades the quality of the controlled phase operator, requiring more applications of carrier and BSB pulses which lengthens the duration of the control. Overall, we empirically find that $N = 4$ strikes a good balance, offering a favorable metrological gain in both number and phase while ensuring a sufficiently high quality of experimental controls.

The metrological gain of the NP states is characterized in a similar manner as grid states using the QPE circuit of Fig. 1E with the following changes. After preparation, the NP state is subjected to phonon shifts and rotations. The shifts are experimentally implemented by initializing the qubit in the $|\downarrow\rangle$ state and repeating $\hat{E}^+$ for ϵ_n times. A rotation $e^{i\epsilon_\phi \hat{n}}$ is then applied by offsetting the phases of all subsequent pulses in software, such that the BSB phase of $\hat{H}_\mathrm{b}$ becomes $\phi_\mathrm{b} \rightarrow \phi_\mathrm{b} + \epsilon_\phi$. Measurements of the conditional operators require a Hadamard rotation applied to the ancilla before and after $C\hat{S}_n$ and $C\hat{S}_\phi$, as the operators act in the $\hat{\sigma}_z$ basis, and the ancillary rotations are also performed in the $\hat{\sigma}_z$ basis.

The variances of number and phase, $\mathrm{V}(\epsilon_\phi)$ and $\mathrm{V}(\epsilon_n)$, are plotted in Fig. 4D for increasing $\langle \hat{n} \rangle$. We first observe that $\mathrm{V}(\epsilon_\phi)$ (blue squares) decreases up to $\langle \hat{n} \rangle = 6$, where it follows the SQL which scales with $1/\langle \hat{n} \rangle$. The variance $\mathrm{V}(\epsilon_n)$ (purple squares) remains significantly below its SQL, which scales as $\langle \hat{n} \rangle$. We also observe that the variance $\mathrm{V}(\epsilon_n)$ is much lower than its respective SQL compared to $\mathrm{V}(\epsilon_\phi)$; this is expected, since the experimentally prepared NP states are only approximate eigenstates of the phase operator but are exact eigenstates of the number operator. We further investigate the metrological gain for simultaneous estimation of number and phase by summing their variances, after rescaling $\mathrm{V}(\epsilon_\phi)$ and $\mathrm{V}(\epsilon_n)$ such that their respective SQLs are equal to 1 (Fig. 4D). The smallest combined variance is obtained for $\langle \hat{n} \rangle = 6$, giving a gain of 3.1(9) dB over the simultaneous SQL.

DISCUSSION

In summary, we demonstrated multiparameter sensing of incompatible observables using a single mode with estimated parameter uncertainties simultaneously reduced below the SQL. This was achieved by a backaction-evading measurement scheme combined with a versatile, high-fidelity quantum control protocol that allows the preparation of highly nonclassical states tailored for measuring small displacements. We prepared grid states and NP states to simultaneously measure position-momentum and NP, respectively. We achieved a metrological gain with the grid states of 5.1(5) dB over the SQL and a gain of 3.1(9) dB for the NP states. In addition, we implemented a multiparameter QPE algorithm to estimate changes in the position and momentum caused by random displacements. The combined variance was reduced below the simultaneous SQL after a sufficient number of measurements, and the variance was further reduced by adaptively varying controllable phases during the experiment.

In addition, this work constitutes the first experimental realization and control of NP states. A polar decomposition into number and phase is a natural representation for devices where intrinsic noise is dominated by dephasing, making these states prime candidates for novel metrology in the presence of noise. For example, NP states can be used in error-corrected quantum metrology, where the precision of estimating a parameter is enhanced by protecting against noise in the other parameter (*44*, *45*). Beyond quantum metrology, these states serve as code states of rotation symmetric codes for error-corrected quantum information processing (*31*, *46*). Measurements of the NP states' stabilizer lifetimes reveal a strong bias (see the Supplementary Materials), suggesting a favorable QEC performance (*47*, *48*). Opportunities exist to enhance the quality of NP states and their measurements. First, the required interactions for preparation and measurement could potentially be improved through light-atom Hamiltonian engineering and optimal control strategies. Second, better designs of NP states, such as Fock spacings and envelopes, could improve performance in the presence of specific noises in devices.

Looking forward, our multiparameter displacement sensor can be used for phase-insensitive force sensing. The adaptive-QPE results of Fig. 3 give an equivalent phase-insensitive force sensitivity of $14.3\mathrm{yN}/\sqrt{\mathrm{Hz}}$ ($1\,\mathrm{yN} = 1 \times 10^{-24}\,\mathrm{N}$), which is comparable to state-of-the-art sensors that rely on prior phase synchronizations between the force and the sensor (see the Supplementary Materials) (*49*, *50*). Our scheme is well suited for quantum logic–enabled photon-recoil spectroscopy (*51*, *52*) to drive narrow linewidth transitions in molecular ions (*53*–*55*) and highly charged ions (*56*, *57*), which can benefit atomic clocks (*58*) and the search for new physics (*59*). Another exciting aspect is the further reduction of our force sensitivity by several orders of magnitude by increasing the sensing duration and using larger ion crystals, which could benefit the search for dark matter (*50*, *60*). Our demonstration is also compatible with photonic-linked trapped-ion devices (*61*), providing an exciting prospect to use an entangled network of sensors to perform long-baseline quantum-enhanced sensing (*62*).

MATERIALS AND METHODS

Experimental control toolbox

The experiments in this work use a combination of red-sideband (RSB) and BSB interactions. These are obtained from stimulated Raman transitions with a 355-nm pulsed laser. A bichromatic field with a frequency difference of $\omega_0 - \omega_m + \delta_\mathrm{r}$ or $\omega_0 + \omega_m + \delta_\mathrm{b}$ gives an RSB or a BSB interaction, respectively, where ω_0 is the qubit frequency and ω_m is the motional frequency. The frequencies δ_r and δ_b are the detunings from the RSB and BSB interactions, respectively. In an interaction picture with respect to the ion's spin and motion, and after several rotating wave approximations, the RSB and BSB Hamiltonians are (*63*)

$$\hat{H}_\mathrm{r} = \frac{\Omega_\mathrm{r}}{2}\hat{\sigma}^+\hat{a}e^{-i\delta_\mathrm{r}}e^{i\phi_\mathrm{r}} + \mathrm{h.c.} \tag{5}$$

$$\hat{H}_{\mathrm{b}} = \frac{\Omega_{\mathrm{b}}}{2}\hat{\sigma}^{+}\hat{a}^{\dagger}e^{-i\delta_{\mathrm{b}}}e^{i\phi_{\mathrm{b}}} + \mathrm{h.c.} \quad (6)$$

where $\hat{\sigma}^{+} = |\uparrow\rangle\langle\downarrow|$ is the Pauli raising operator, ϕ_r and ϕ_b are controllable RSB and BSB phases. An SDF is obtained by simultaneously applying $\hat{H}_{\mathrm{r}}$ and $\hat{H}_{\mathrm{b}}$ with $\delta_{\mathrm{r}} = \delta_{\mathrm{b}} = 0$ and $\Omega = \Omega_{\mathrm{r}} = \Omega_{\mathrm{b}}$, which results in

$$\hat{H}_{\mathrm{SDF}} = \frac{\Omega}{2}\hat{\sigma}_{\phi_s}\left(\hat{a}^{\dagger}e^{-i\phi_m} + \hat{a}e^{i\phi_m}\right) \quad (7)$$

where $\hat{\sigma}_{\phi_s} = \left[\hat{\sigma}_x\cos(\phi_s) + \hat{\sigma}_y\sin(\phi_s)\right]$, $\phi_s = (\phi_r + \phi_b)/2$ is a phase associated with the spin, and $\phi_m = (\phi_r - \phi_b)/2$ is a phase associated with the motion. Applying $\hat{H}_{\mathrm{SDF}}$ for a duration t gives a displacement conditioned on the state of the spin, $\hat{D}(\hat{\sigma}_{\phi_s}\alpha)$, whose operation can be written as

$$\hat{D}(\hat{\sigma}_{\phi_s}\alpha) = |+\rangle\langle+| \otimes \hat{D}(\alpha) + |-\rangle\langle-| \otimes \hat{D}^{\dagger}(\alpha) \quad (8)$$

where $|\pm\rangle$ are the eigenstates of $\hat{\sigma}_{\phi_s}$ and $\alpha = -i\Omega t e^{-i\phi_m}/2$. The magnitude of the displacement, $|\alpha|$, is set by varying the duration t for a given Rabi frequency, Ω. The phase of the displacement, $\arg(\alpha)$, is set by the motional phase, ϕ_m, which can be controlled by adjusting the phase of the radio-frequency driving the AOM in the path of the Raman beam.

Preparing sensing states

The sensing states in this work are prepared via optimal control by applying $\hat{H}_{\mathrm{SDF}}$ of Eq. 7 with dynamically modulated phases $\phi_s(t)$ and $\phi_m(t)$ (*34*). The modulation waveforms are obtained through a numerical optimization procedure using Q-CTRL's graph-based optimizer (Boulder Opal) (*64*, *65*). The numerical optimizer minimizes the cost function

$$C = (1 - \mathcal{F}) + \epsilon\frac{T}{T_{\max}} \quad (9)$$

where $\mathcal{F}$ is a fidelity, T is the duration of the pulse, and $T_{\max}$ is the maximum allowed duration. In this way, the duration of the pulse is minimized, while the convergence criterion ϵ ensures that $1 - \mathcal{F} \lesssim \epsilon$. We define the fidelity as the overlap between the generated state and the target state $|\psi_{\mathrm{t}}\rangle$ (see the Supplementary Materials for definitions of the grid and NP states), $\mathcal{F} = |\langle\downarrow, \psi_{\mathrm{t}}|\,\hat{U}\,|\downarrow, 0\rangle|^2$, with $\hat{U} = \exp\left[-i\int_0^T dt\hat{H}_{\mathrm{SDF}}(t)\right]$.

The phase modulations of $\phi_s(t)$ and $\phi_m(t)$ are represented as a piece-wise constant signal with N_{opt} optimizable segments. We add several constraints to the segments to avoid signal line distortions from the finite-bandwidth of the AOMs. First, the slew rate $|\phi_{i+1} - \phi_i| < \mathrm{SR}$ limits the maximum difference of the values of two consecutive segments. Second, the optimizable segments are filtered with a sinc filter, and N_{seg} segments are resampled from the filtered signal. We set $N_{\mathrm{opt}} = 50$ ($N_{\mathrm{opt}} = 30$) for the grid states (NP states), and resample $N_{\mathrm{seg}} = 150$ segments for all states. The slew rate is set to $\mathrm{SR} = 1.5$, and the cutoff frequency of the sinc filter is $f_c \times T = 2\pi \times 15$.

Dephasing in the motional degrees of freedom

The two common sources of decoherence in the motional modes of trapped ions are heating and dephasing [see (*63*) for a detailed discussion]. In our experiment, we measure a heating rate of 0.2 phonons/s (*66*), which is negligible given the typical duration of an experiment. The dominant source of noise is therefore motional dephasing, which we describe in greater detail below.

Motional dephasing, modeled by the noisy Hamiltonian term $\nu(t)\hat{a}^{\dagger}\hat{a}$ with stochastic $\nu(t)$, describes random fluctuations of the motional mode's frequency. In trapped ions, these fluctuations arise from noise in the confining potential which, for radial modes of motion, originates from noise in the amplitude of the trapping radio frequency signal due to thermal fluctuations in the resonator and electronic noise in the controller hardware. In our setup, the amplitude of the trapping RF voltage is actively stabilized by a closed-loop feedback circuit. The amplitude is first measured from the RF signal that is capacitively coupled to opposing blades that are radially symmetric with respect to the ion. The amplitude is then stabilized by a custom-built analog PID, whose output regulates a variable voltage attenuator in the path of the RF trapping voltage connected to the trap. With this, we measure a motional coherence time of $T_2^* \approx 50\mathrm{ms}$ from a Ramsey sequence between Fock states $|0\rangle$ and $|1\rangle$ (*34*). Increasing the coherence time is ongoing work, with potential hardware improvements including better thermal stabilization and lower electronic noise.

Supplementary Materials

This PDF file includes:

Supplementary Materials and Methods
Supplementary Text
Tables S1 and S2
Figs. S1 to S16
References

REFERENCES AND NOTES

1. J. Aasi, J. Abadie, B. P. Abbott, R. Abbott, T. D. Abbott, M. R. Abernathy, C. Adams, T. Adams, P. Addesso, R. X. Adhikari, C. Affeldt, O. D. Aguiar, P. Ajith, B. Allen, E. Amador Ceron, D. Amariutei, S. B. Anderson, W. G. Anderson, K. Arai, M. C. Araya, C. Arceneaux, S. Ast, S. M. Aston, D. Atkinson, P. Aufmuth, C. Aulbert, L. Austin, B. E. Aylott, S. Babak, P. T. Baker, S. Ballmer, Y. Bao, J. C. Barayoga, D. Barker, B. Barr, L. Barsotti, M. A. Barton, I. Bartos, R. Bassiri, J. Batch, J. Bauchrowitz, B. Behnke, A. S. Bell, C. Bell, G. Bergmann, J. M. Berliner, A. Bertolini, J. Betzwieser, N. Beveridge, P. T. Beyersdorf, T. Bhadbhade, I. A. Bilenko, G. Billingsley, J. Birch, S. Biscans, E. Black, J. K. Blackburn, L. Blackburn, D. Blair, B. Bland, O. Bock, T. P. Bodiya, C. Bogan, C. Bond, R. Bork, M. Born, S. Bose, J. Bowers, P. R. Brady, V. B. Braginsky, J. E. Brau, J. Breyer, D. O. Bridges, M. Brinkmann, M. Britzger, A. F. Brooks, D. A. Brown, D. D. Brown, K. Buckland, F. Brückner, B. C. Buchler, A. Buonanno, J. Burguet-Castell, R. L. Byer, L. Cadonati, J. B. Camp, P. Campsie, K. Cannon, J. Cao, C. D. Capano, L. Carbone, S. Caride, A. D. Castiglia, S. Caudill, M. Cavaglià, C. Cepeda, T. Chalermsongsak, S. Chao, P. Charlton, X. Chen, Y. Chen, H. S. Cho, J. H. Chow, N. Christensen, Q. Chu, S. S. Y. Chua, C. T. Y. Chung, G. Ciani, F. Clara, D. E. Clark, J. A. Clark, M. Constancio Junior, D. Cook, T. R. Corbitt, M. Cordier, N. Cornish, A. Corsi, C. A. Costa, M. W. Coughlin, S. Countryman, P. Couvares, D. M. Coward, M. Cowart, D. C. Coyne, K. Craig, J. D. E. Creighton, T. D. Creighton, A. Cumming, L. Cunningham, K. Dahl, M. Damjanic, S. L. Danilishin, K. Danzmann, B. Daudert, H. Daveloza, G. S. Davies, E. J. Daw, T. Dayanga, E. Deleeuw, T. Denker, T. Dent, V. Dergachev, R. DeRosa, R. DeSalvo, S. Dhurandhar, I. di Palma, M. Díaz, A. Dietz, F. Donovan, K. L. Dooley, S. Doravari, S. Drasco, R. W. P. Drever, J. C. Driggers, Z. du, J. C. Dumas, S. Dwyer, T. Eberle, M. Edwards, A. Effler, P. Ehrens, S. S. Eikenberry, R. Engel, R. Essick, T. Etzel, K. Evans, M. Evans, T. Evans, M. Factourovich, S. Fairhurst, Q. Fang, B. F. Farr, W. Farr, M. Favata, D. Fazi, H. Fehrmann, D. Feldbaum, L. S. Finn, R. P. Fisher, S. Foley, E. Forsi, N. Fotopoulos, M. Frede, M. A. Frei, Z. Frei, A. Freise, R. Frey, T. T. Fricke, D. Friedrich, P. Fritschel, V. V. Frolov, M. K. Fujimoto, P. J. Fulda, M. Fyffe, J. Gair, J. Garcia, N. Gehrels, G. Gelencser, L. Á. Gergely, S. Ghosh, J. A. Giaime, S. Giampanis, K. D. Giardina, S. Gil-Casanova, C. Gill, J. Gleason, E. Goetz, G. González, N. Gordon, M. L. Gorodetsky, S. Gossan, S. Goßler, C. Graef, P. B. Graff, A. Grant, S. Gras, C. Gray, R. J. S. Greenhalgh, A. M. Gretarsson, C. Griffo, H. Grote, K. Grover, S. Grunewald, C. Guido, E. K. Gustafson, R. Gustafson, D. Hammer, G. Hammond, J. Hanks, C. Hanna, J. Hanson, K. Haris, J. Harms, G. M. Harry, I. W. Harry, E. D. Harstad, M. T. Hartman, K. Haughian, K. Hayama, J. Heefner, M. C. Heintze, M. A. Hendry, I. S. Heng, A. W. Heptonstall, M. Heurs, M. Hewitson, S. Hild, D. Hoak, K. A. Hodge, K. Holt, M. Holtrop, T. Hong, S. Hooper, J. Hough, E. J. Howell, V. Huang, E. A. Huerta, B. Hughey, S. H. Huttner, M. Huynh, T. Huynh-Dinh, D. R. Ingram, R. Inta, T. Isogai, A. Ivanov, B. R. Iyer, K. Izumi, M. Jacobson, E. James, H. Jang, Y. J. Jang,

E. Jesse, W. W. Johnson, D. Jones, D. I. Jones, R. Jones, L. Ju, P. Kalmus, V. Kalogera, S. Kandhasamy, G. Kang, J. B. Kanner, R. Kasturi, E. Katsavounidis, W. Katzman, H. Kaufer, K. Kawabe, S. Kawamura, F. Kawazoe, D. Keitel, D. B. Kelley, W. Kells, D. G. Keppel, A. Khalaidovski, F. Y. Khalili, E. A. Khazanov, B. K. Kim, C. Kim, K. Kim, N. Kim, Y. M. Kim, P. J. King, D. L. Kinzel, J. S. Kissel, S. Klimenko, J. Kline, K. Kokeyama, V. Kondrashov, S. Koranda, W. Z. Korth, D. Kozak, C. Kozameh, A. Kremin, V. Kringel, B. Krishnan, C. Kucharczyk, G. Kuehn, P. Kumar, R. Kumar, B. J. Kuper, R. Kurdyumov, P. Kwee, P. K. Lam, M. Landry, B. Lantz, P. D. Lasky, C. Lawrie, A. Lazzarini, A. le Roux, P. Leaci, C. H. Lee, H. K. Lee, H. M. Lee, J. Lee, J. R. Leong, B. Levine, V. Lhuillier, A. C. Lin, V. Litvine, Y. Liu, Z. Liu, N. A. Lockerbie, D. Lodhia, K. Loew, J. Logue, A. L. Lombardi, M. Lormand, J. Lough, M. Lubinski, H. Lück, A. P. Lundgren, J. Macarthur, E. Macdonald, B. Machenschalk, M. MacInnis, D. M. Macleod, F. Magaña-Sandoval, M. Mageswaran, K. Mailand, G. Manca, I. Mandel, V. Mandic, S. Márka, Z. Márka, A. S. Markosyan, E. Maros, I. W. Martin, R. M. Martin, D. Martinov, J. N. Marx, K. Mason, F. Matichard, L. Matone, R. A. Matzner, N. Mavalvala, G. May, G. Mazzolo, K. McAuley, R. McCarthy, D. E. McClelland, S. C. McGuire, G. McIntyre, J. McIver, G. D. Meadors, M. Mehmet, T. Meier, A. Melatos, G. Mendell, R. A. Mercer, S. Meshkov, C. Messenger, M. S. Meyer, H. Miao, J. Miller, C. M. F. Mingarelli, S. Mitra, V. P. Mitrofanov, G. Mitselmakher, R. Mittleman, B. Moe, F. Mokler, S. R. P. Mohapatra, D. Moraru, G. Moreno, T. Mori, S. R. Morriss, K. Mossavi, C. M. Mow-Lowry, C. L. Mueller, G. Mueller, S. Mukherjee, A. Mullavey, J. Munch, D. Murphy, P. G. Murray, A. Mytidis, D. Nanda Kumar, T. Nash, R. Nayak, V. Necula, G. Newton, T. Nguyen, E. Nishida, A. Nishizawa, A. Nitz, D. Nolting, M. E. Normandin, L. K. Nuttall, J. O'Dell, B. O'Reilly, R. O'Shaughnessy, E. Ochsner, E. Oelker, G. H. Ogin, J. J. Oh, S. H. Oh, F. Ohme, P. Oppermann, C. Osthelder, C. D. Ott, D. J. Ottaway, R. S. Ottens, J. Ou, H. Overmier, B. J. Owen, C. Padilla, A. Pai, Y. Pan, C. Pankow, M. A. Papa, H. Paris, W. Parkinson, M. Pedraza, S. Penn, C. Peralta, A. Perreca, M. Phelps, M. Pickenpack, V. Pierro, I. M. Pinto, M. Pitkin, H. J. Pletsch, J. Pöld, F. Postiglione, C. Poux, V. Predoi, T. Prestegard, L. R. Price, M. Prijatelj, S. Privitera, L. G. Prokhorov, O. Puncken, V. Quetschke, E. Quintero, R. Quitzow-James, F. J. Raab, H. Radkins, P. Raffai, S. Raja, M. Rakhmanov, C. Ramet, V. Raymond, C. M. Reed, T. Reed, S. Reid, D. H. Reitze, R. Riesen, K. Riles, M. Roberts, N. A. Robertson, E. L. Robinson, S. Roddy, C. Rodriguez, L. Rodriguez, M. Rodruck, J. G. Rollins, J. H. Romie, C. Röver, S. Rowan, A. Rüdiger, K. Ryan, F. Salemi, L. Sammut, V. Sandberg, J. Sanders, S. Sankar, V. Sannibale, L. Santamaría, I. Santiago-Prieto, G. Santostasi, B. S. Sathyaprakash, P. R. Saulson, R. L. Savage, R. Schilling, R. Schnabel, R. M. S. Schofield, D. Schuette, B. Schulz, B. F. Schutz, P. Schwinberg, J. Scott, S. M. Scott, F. Seifert, D. Sellers, A. S. Sengupta, A. Sergeev, D. A. Shaddock, M. S. Shahriar, M. Shaltev, Z. Shao, B. Shapiro, P. Shawhan, D. H. Shoemaker, T. L. Sidery, X. Siemens, D. Sigg, D. Simakov, A. Singer, L. Singer, A. M. Sintes, G. R. Skelton, B. J. J. Slagmolen, J. Slutsky, J. R. Smith, M. R. Smith, R. J. E. Smith, N. D. Smith-Lefebvre, E. J. Son, B. Sorazu, T. Souradeep, M. Stefszky, E. Steinert, J. Steinlechner, S. Steinlechner, S. Steplewski, D. Stevens, A. Stochino, R. Stone, K. A. Strain, S. E. Strigin, A. S. Stroeer, A. L. Stuver, T. Z. Summerscales, S. Susmithan, P. J. Sutton, G. Szeifert, D. Talukder, D. B. Tanner, S. P. Tarabrin, R. Taylor, M. Thomas, P. Thomas, K. A. Thorne, K. S. Thorne, E. Thrane, V. Tiwari, K. V. Tokmakov, C. Tomlinson, C. V. Torres, C. I. Torrie, G. Traylor, M. Tse, D. Ugolini, C. S. Unnikrishnan, H. Vahlbruch, M. Vallisneri, M. V. van der Sluys, A. A. van Veggel, S. Vass, R. Vaulin, A. Vecchio, P. J. Veitch, J. Veitch, K. Venkateswara, S. Verma, R. Vincent-Finley, S. Vitale, T. Vo, C. Vorvick, W. D. Vousden, S. P. Vyatchanin, A. Wade, L. Wade, M. Wade, S. J. Waldman, L. Wallace, Y. Wan, M. Wang, J. Wang, X. Wang, A. Wanner, R. L. Ward, M. Was, M. Weinert, A. J. Weinstein, R. Weiss, T. Welborn, L. Wen, P. Wessels, M. West, T. Westphal, K. Wette, J. T. Whelan, S. E. Whitcomb, A. G. Wiseman, D. J. White, B. F. Whiting, K. Wiesner, C. Wilkinson, P. A. Willems, L. Williams, R. Williams, T. Williams, J. L. Willis, B. Willke, M. Wimmer, L. Winkelmann, W. Winkler, C. C. Wipf, H. Wittel, G. Woan, R. Wooley, J. Worden, J. Yablon, I. Yakushin, H. Yamamoto, C. C. Yancey, H. Yang, D. Yeaton-Massey, S. Yoshida, H. Yum, M. Zanolin, F. Zhang, L. Zhang, C. Zhao, H. Zhu, X. J. Zhu, N. Zotov, M. E. Zucker, J. Zweizig, Enhanced sensitivity of the LIGO gravitational wave detector by using squeezed states of light. *Nat. Photon.s* **7**, 613–619 (2013).

2. B. Abbott, R. Abbott, T. Abbott, M. R. Abernathy, F. Acernese, K. Ackley, C. Adams, T. Adams, P. Addesso, LIGO Scientific Collaboration and Virgo Collaboration, Observation of gravitational waves from a binary black hole merger. *Phys. Rev. Lett.* **116**, 061102 (2016).
3. V. Giovannetti, S. Lloyd, L. Maccone, Quantum-enhanced measurements: Beating the standard quantum limit. *Science* **306**, 1330–1336 (2004).
4. M. Tse, H. Yu, N. Kijbunchoo, A. Fernandez-Galiana, P. Dupej, L. Barsotti, C. Blair, D. Brown, S. Dwyer, A. Effler, M. Evans, P. Fritschel, V. V. Frolov, A. C. Green, G. L. Mansell, F. Matichard, N. Mavalvala, D. E. McClelland, L. McCuller, T. McRae, J. Miller, A. Mullavey, E. Oelker, I. Y. Phinney, D. Sigg, B. J. J. Slagmolen, T. Vo, R. L. Ward, C. Whittle, R. Abbott, C. Adams, R. X. Adhikari, A. Ananyeva, S. Appert, K. Arai, J. S. Areeda, Y. Asali, S. M. Aston, C. Austin, A. M. Baer, M. Ball, S. W. Ballmer, S. Banagiri, D. Barker, J. Bartlett, B. K. Berger, J. Betzwieser, D. Bhattacharjee, G. Billingsley, S. Biscans, R. M. Blair, N. Bode, P. Booker, R. Bork, A. Bramley, A. F. Brooks, A. Buikema, C. Cahillane, K. C. Cannon, X. Chen, A. A. Ciobanu, F. Clara, S. J. Cooper, K. R. Corley, S. T. Countryman, P. B. Covas, D. C. Coyne, L. E. H. Datrier, D. Davis, C. di Fronzo, J. C. Driggers, T. Etzel, T. M. Evans, J. Feicht, P. Fulda, M. Fyffe, J. A. Giaime, K. D. Giardina, P. Godwin, E. Goetz, S. Gras, C. Gray, R. Gray, A. Gupta, E. K. Gustafson, R. Gustafson, J. Hanks, J. Hanson, T. Hardwick, R. K. Hasskew, M. C. Heintze, A. F. Helmling-Cornell, N. A. Holland, J. D. Jones, S. Kandhasamy, S. Karki, M. Kasprzack, K. Kawabe, P. J. King, J. S. Kissel, R. Kumar, M. Landry, B. B. Lane, B. Lantz, M. Laxen, Y. K. Lecoeuche, J. Leviton, J. Liu, M. Lormand, A. P. Lundgren, R. Macas, M. MacInnis, D. M. Macleod, S. Márka, Z. Márka, D. V. Martynov, K. Mason, T. J. Massinger, R. McCarthy, S. McCormick, J. McIver, G. Mendell, K. Merfeld, E. L. Merilh, F. Meylahn, T. Mistry, R. Mittleman, G. Moreno, C. M. Mow-Lowry, S. Mozzon, T. J. N. Nelson, P. Nguyen, L. K. Nuttall, J. Oberling, R. J. Oram, B. O'Reilly, C. Osthelder, D. J. Ottaway, H. Overmier, J. R. Palamos, W. Parker, E. Payne, A. Pele, C. J. Perez, M. Pirello, H. Radkins, K. E. Ramirez, J. W. Richardson, K. Riles, N. A. Robertson, J. G. Rollins, C. L. Romel, J. H. Romie, M. P. Ross, K. Ryan, T. Sadecki, E. J. Sanchez, L. E. Sanchez, T. R. Saravanan, R. L. Savage, D. Schaetzl, R. Schnabel, R. M. S. Schofield, E. Schwartz, D. Sellers, T. J. Shaffer, J. R. Smith, S. Soni, B. Sorazu, A. P. Spencer, K. A. Strain, L. Sun, M. J. Szczepańczyk, M. Thomas, P. Thomas, K. A. Thorne, K. Toland, C. I. Torrie, G. Traylor, A. L. Urban, G. Vajente, G. Valdes, D. C. Vander-Hyde, P. J. Veitch, K. Venkateswara, G. Venugopalan, A. D. Viets, C. Vorvick, M. Wade, J. Warner, B. Weaver, R. Weiss, B. Willke, C. C. Wipf, L. Xiao, H. Yamamoto, M. J. Yap, H. Yu, L. Zhang, M. E. Zucker, J. Zweizig, Quantum-enhanced advanced LIGO detectors in the era of gravitational-wave astronomy. *Phys. Rev. Lett.* **123**, 231107 (2019).
5. A. D. Ludlow, M. M. Boyd, J. Ye, E. Peik, P. O. Schmidt, Optical atomic clocks. *Rev. Mod. Phys.* **87**, 637–701 (2015).
6. M. A. Taylor, J. Janousek, V. Daria, J. Knittel, B. Hage, H.-A. Bachor, W. P. Bowen, Biological measurement beyond the quantum limit. *Nat. Photon.* **7**, 229–233 (2013).
7. M. A. Taylor, J. Janousek, V. Daria, J. Knittel, B. Hage, H.-A. Bachor, W. P. Bowen, Subdiffraction-limited quantum imaging within a living cell. *Phys. Rev. X* **4**, 011017 (2014).
8. K. M. Backes, D. A. Palken, S. A. Kenany, B. M. Brubaker, S. B. Cahn, A. Droster, G. C. Hilton, S. Ghosh, H. Jackson, S. K. Lamoreaux, A. F. Leder, K. W. Lehnert, S. M. Lewis, M. Malnou, R. H. Maruyama, N. M. Rapidis, M. Simanovskaia, S. Singh, D. H. Speller, I. Urdinaran, L. R. Vale, E. C. van Assendelft, K. V. Bibber, H. Wang, A quantum enhanced search for dark matter axions. *Nature* **590**, 238–242 (2021).
9. W. Heisenberg, Über den anschaulichen Inhalt der quantentheoretischen Kinematik und Mechanik. *Zeitschrift für Physik* **43**, 172–198 (1927).
10. M. Ozawa, Uncertainty relations for joint measurements of noncommuting observables. *Phys. Lett. A* **320**, 367–374 (2004).
11. K. Jensen, W. Wasilewski, H. Krauter, T. Fernholz, B. M. Nielsen, M. Owari, M. B. Plenio, A. Serafini, M. M. Wolf, E. S. Polzik, Quantum memory for entangled continuous-variable states. *Nat. Phys.* **7**, 13–16 (2011).
12. C. F. Ockeloen-Korppi, E. Damskägg, J.-M. Pirkkalainen, M. Asjad, A. A. Clerk, F. Massel, M. J. Woolley, M. A. Sillanpää, Stabilized entanglement of massive mechanical oscillators. *Nature* **556**, 478–482 (2018).
13. S. Barzanjeh, E. S. Redchenko, M. Peruzzo, M. Wulf, D. P. Lewis, G. Arnold, J. M. Fink, Stationary entangled radiation from micromechanical motion. *Nature* **570**, 480–483 (2019).
14. J. Qin, Y.-H. Deng, H.-S. Zhong, L.-C. Peng, H. Su, Y.-H. Luo, J.-M. Xu, D. Wu, S.-Q. Gong, H.-L. Liu, H. Wang, M.-C. Chen, L. Li, N.-L. Liu, C.-Y. Lu, J.-W. Pan, Unconditional and robust quantum metrological advantage beyond N00N states. *Phys. Rev. Lett.* **130**, 070801 (2023).
15. W. S. Leong, M. Xin, Z. Chen, Y. Wang, S.-Y. Lan, Creation of two-mode squeezed states in atomic mechanical oscillators. *Phys. Rev. Lett.* **131**, 193601 (2023).
16. J. Metzner, A. Quinn, S. Brudney, I. D. Moore, S. C. Burd, D. J. Wineland, D. T. C. Allcock, Two-mode squeezing and SU(1, 1) interferometry with trapped ions. *Phys. Rev. A* **110**, 022613 (2024).
17. M. G. Genoni, M. G. A. Paris, G. Adesso, H. Nha, P. L. Knight, M. S. Kim, Optimal estimation of joint parameters in phase space. *Phys. Rev. A* **87**, 012107 (2013).
18. J. Cao, X. Li, T. Mao, W. Xu, L. You, Joint estimation of a two-phase spin rotation beyond classical limit. *Phys. Rev. Lett.* **135**, 023403 (2023).
19. Y. Li, X. Cheng, L. Wang, X. Zhao, W. Hou, Y. Li, K. Rehan, M. Zhu, L. Yan, X. Qin, X. Peng, H. Yuan, Y. Lin, J. Du, Multi-parameter quantum metrology with stabilized multi-mode squeezed state. arXiv:2312.10379 [quant-ph] (2023).
20. Y. Aharonov, H. Pendleton, A. Petersen, Modular variables in quantum theory. *Int. J. Theor. Phys* **2**, 213–230 (1969).
21. D. Gottesman, A. Kitaev, J. Preskill, Encoding a qubit in an oscillator. *Phys. Rev. A* **64**, 012310 (2001).
22. A. Ketterer, A. Keller, S. P. Walborn, T. Coudreau, P. Milman, Quantum information processing in phase space: A modular variables approach. *Phys. Rev. A* **94**, 022325 (2016).
23. K. Duivenvoorden, B. M. Terhal, D. Weigand, Single-mode displacement sensor. *Phys. Rev. A* **95**, 012305 (2017).
24. C. Flühmann, V. Negnevitsky, M. Marinelli, J. Home, Sequential modular position and momentum measurements of a trapped ion mechanical oscillator. *Phys. Rev. X* **8**, 021001 (2018).

25. C. Flühmann, T. L. Nguyen, M. Marinelli, V. Negnevitsky, K. Mehta, J. P. Home, Encoding a qubit in a trapped-ion mechanical oscillator. *Nature* **566**, 513–517 (2019).
26. P. Campagne-Ibarcq, A. Eickbusch, S. Touzard, E. Zalys-Geller, N. E. Frattini, V. V. Sivak, P. Reinhold, S. Puri, S. Shankar, R. J. Schoelkopf, L. Frunzio, M. Mirrahimi, M. H. Devoret, Quantum error correction of a qubit encoded in grid states of an oscillator. *Nature* **584**, 368–372 (2020).
27. B. de Neeve, T.-L. Nguyen, T. Behrle, J. P. Home, Error correction of a logical grid state qubit by dissipative pumping. *Nat. Phys.* **18**, 296–300 (2022).
28. A. Eickbusch, V. Sivak, A. Z. Ding, S. S. Elder, S. R. Jha, J. Venkatraman, B. Royer, S. M. Girvin, R. J. Schoelkopf, M. H. Devoret, Fast universal control of an oscillator with weak dispersive coupling to a qubit. *Nat. Phys.* **18**, 1464–1469 (2022).
29. V. V. Sivak, A. Eickbusch, B. Royer, S. Singh, I. Tsioutsios, S. Ganjam, A. Miano, B. L. Brock, A. Z. Ding, L. Frunzio, S. M. Girvin, R. J. Schoelkopf, M. H. Devoret, Real-time quantum error correction beyond break-even. *Nature* **616**, 50–55 (2023).
30. A. Kawasaki, R. Ide, H. Brunel, T. Suzuki, R. Nehra, K. Nakashima, T. Kashiwazaki, A. Inoue, T. Umeki, F. China, M. Yabuno, S. Miki, H. Terai, T. Yamashima, A. Sakaguchi, K. Takase, M. Endo, W. Asavanant, A. Furusawa, Broadband generation and tomography of non-Gaussian states for ultra-fast optical quantum processors. *Nat. Commun.* **15**, 9075 (2024).
31. A. L. Grimsmo, J. Combes, B. Q. Baragiola, Quantum computing with rotation-symmetric bosonic codes. *Phys. Rev. X* **10**, 011058 (2020).
32. R. J. MacDonell, T. Navickas, T. F. Wohlers-Reichel, C. H. Valahu, A. D. Rao, M. J. Millican, M. A. Currington, M. J. Biercuk, T. R. Tan, C. Hempel, I. Kassal, Predicting molecular vibronic spectra using time-domain analog quantum simulation. *Chem. Sci.* **14**, 9439–9451 (2023).
33. C. H. Valahu, V. C. Olaya-Agudelo, R. J. MacDonell, T. Navickas, A. D. Rao, M. J. Millican, J. B. Pérez-Sánchez, J. Yuen-Zhou, M. J. Biercuk, C. Hempel, T. R. Tan, I. Kassal, Direct observation of geometric-phase interference in dynamics around a conical intersection. *Nat. Chem.* **15**, 1503–1508 (2023).
34. V. Matsos, C. Valahu, T. Navickas, A. Rao, M. Millican, X. Kolesnikow, M. Biercuk, T. Tan, Robust and deterministic preparation of bosonic logical states in a trapped ion. *Phys. Rev. Lett.* **133**, 050602 (2024).
35. N. Wiebe, C. Granade, Efficient Bayesian phase estimation. *Phys. Rev. Lett.* **117**, 010503 (2016).
36. C. Bonato, M. S. Blok, H. T. Dinani, D. W. Berry, M. L. Markham, D. J. Twitchen, R. Hanson, Optimized quantum sensing with a single electron spin using real-time adaptive measurements. *Nat. Nanotechnol.* **11**, 247–252 (2015).
37. D. W. Berry, H. M. Wiseman, Optimal states and almost optimal adaptive measurements for quantum interferometry. *Phys. Rev. Lett.* **85**, 5098–5101 (2000).
38. Z. Huang, K. R. Motes, P. M. Anisimov, J. P. Dowling, D. W. Berry, Adaptive phase estimation with two-mode squeezed vacuum and parity measurement. *Phys. Rev. A* **95**, 053837 (2017).
39. B. Royer, S. Singh, S. Girvin, Stabilization of finite-energy Gottesman-Kitaev-preskill states. *Phys. Rev. Lett.* **125**, 260509 (2020).
40. V. G. Matsos, C. H. Valahu, M. J. Millican, T. Navickas, X. C. Kolesnikow, M. J. Biercuk, T. R. Tan, T. R. Tan, Universal quantum gate set for Gottesman-Kitaev-Preskill logical qubits. *Nat. Phys.*, 10.1038/s41567-025-03002-8 (2025).
41. A. Holevo, Covariant measurements and uncertainty relations. *Rep. Math. Phys.* **16**, 385–400 (1979).
42. L. Susskind, J. Glogower, Quantum mechanical phase and time operator. *Phys. Phys. Fiz.* **1**, 49–61 (1964).
43. M. Um, J. Zhang, D. Lv, Y. Lu, S. An, J.-N. Zhang, H. Nha, M. S. Kim, K. Kim, Phonon arithmetic in a trapped ion system. *Nat. Commun.* **7**, 11410 (2016).
44. E. Kessler, I. Lovchinsky, A. Sushkov, M. Lukin, Quantum error correction for metrology. *Phys. Rev. Lett.* **112**, 150802 (2014).
45. Y. Ouyang, E. T. Campbell, Trade-offs on number and phase shift resilience in bosonic quantum codes. *IEEE Trans. Inform. Theory* **67**, 6644–6652 (2021).
46. P. Leviant, Q. Xu, L. Jiang, S. Rosenblum, Quantum capacity and codes for the bosonic loss-dephasing channel. *Quantum* **6**, 821 (2022).
47. S. Puri, L. St-Jean, J. A. Gross, A. Grimm, N. E. Frattini, P. S. Iyer, A. Krishna, S. Touzard, L. Jiang, A. Blais, S. T. Flammia, S. M. Girvin, Bias-preserving gates with stabilized cat qubits. *Sci. Adv.* **6**, 34 (2020).
48. H. Putterman, K. Noh, C. T. Hann, G. S. MacCabe, S. Aghaeimeibodi, R. N. Patel, M. Lee, W. M. Jones, H. Moradinejad, R. Rodriguez, N. Mahuli, J. Rose, J. C. Owens, H. Levine, E. Rosenfeld, P. Reinhold, L. Moncelsi, J. A. Alcid, N. Alidoust, P. Arrangoiz-Arriola, J. Barnett, P. Bienias, H. A. Carson, C. Chen, L. Chen, H. Chinkezian, E. M. Chisholm, M.-H. Chou, A. Clerk, A. Clifford, R. Cosmic, A. V. Curiel, E. Davis, L. DeLorenzo, J. M. D'Ewart, A. Diky, N. D'Souza, P. T. Dumitrescu, S. Eisenmann, E. Elkhouly, G. Evenbly, M. T. Fang, Y. Fang, M. J. Fling, W. Fon, G. Garcia, A. V. Gorshkov, J. A. Grant, M. J. Gray, S. Grimberg, A. L. Grimsmo, A. Haim, J. Hand, Y. He, M. Hernandez, D. Hover, J. S. C. Hung, M. Hunt, J. Iverson, I. Jarrige, J.-C. Jaskula, L. Jiang, M. Kalaee, R. Karabalin, P. J. Karalekas, A. J. Keller, A. Khalajhedayati, A. Kubica, H. Lee, C. Leroux, S. Lieu, V. Ly, K. V. Madrigal, G. Marcaud, G. McCabe, C. Miles, A. Milsted, J. Minguzzi, A. Mishra, B. Mukherjee, M. Naghiloo, E. Oblepias, G. Ortuno, J. Pagdilao, N. Pancotti, A. Panduro, J. Paquette, M. Park, G. A. Peairs, D. Perello, E. C. Peterson, S. Ponte, J. Preskill, J. Qiao, G. Refael, R. Resnick, A. Retzker, O. A. Reyna, M. Runyan, C. A. Ryan, A. Sahmoud, E. Sanchez, R. Sanil, K. Sankar, Y. Sato, T. Scaffidi, S. Siavoshi, P. Sivarajah, T. Skogland, C.-J. Su, L. J. Swenson, S. M. Teo, A. Tomada, G. Torlai, E. A. Wollack, Y. Ye, J. A. Zerrudo, K. Zhang, F. G. S. L. Brandão, M. H. Matheny, O. Painter, Hardware-efficient quantum error correction using concatenated bosonic qubits. *Nature* **638**, 927–934 (2024).
49. M. Affolter, K. A. Gilmore, J. E. Jordan, J. J. Bollinger, Phase-coherent sensing of the center-of-mass motion of trapped-ion crystals. *Phys. Rev. A* **102**, 052609 (2020).
50. K. A. Gilmore, M. Affolter, R. J. Lewis-Swan, D. Barberena, E. Jordan, A. M. Rey, J. J. Bollinger, Quantum-enhanced sensing of displacements and electric fields with two-dimensional trapped-ion crystals. *Science* **373**, 673–678 (2021).
51. C. Hempel, B. P. Lanyon, P. Jurcevic, R. Gerritsma, R. Blatt, C. F. Roos, Entanglement-enhanced detection of single-photon scattering events. *Nat. Photon.* **7**, 630–633 (2013).
52. Y. Wan, F. Gebert, J. B. Wübbena, N. Scharnhorst, S. Amairi, I. D. Leroux, B. Hemmerling, N. Lörch, K. Hammerer, P. O. Schmidt, Precision spectroscopy by photon-recoil signal amplification. *Nat. Commun.* **5**, 3096 (2014).
53. F. Wolf, Y. Wan, J. C. Heip, F. Gebert, C. Shi, P. O. Schmidt, Non-destructive state detection for quantum logic spectroscopy of molecular ions. *Nature* **530**, 457–460 (2016).
54. C.-W. Chou, C. Kurz, D. B. Hume, P. N. Plessow, D. R. Leibrandt, D. Leibfried, Preparation and coherent manipulation of pure quantum states of a single molecular ion. *Nature* **545**, 203–207 (2017).
55. M. Sinhal, Z. Meir, K. Najafian, G. Hegi, S. Willitsch, Quantum-nondemolition state detection and spectroscopy of single trapped molecules. *Science* **367**, 1213–1218 (2020).
56. M. G. Kozlov, M. S. Safronova, J. R. Crespo López-Urrutia, P. O. Schmidt, Highly charged ions: Optical clocks and applications in fundamental physics. *Rev. Mod. Phys.* **90**, 045005 (2018).
57. P. Micke, T. Leopold, S. A. King, E. Benkler, L. J. Spieß, L. Schmöger, M. Schwarz, J. R. C. López-Urrutia, P. O. Schmidt, Coherent laser spectroscopy of highly charged ions using quantum logic. *Nature* **578**, 60–65 (2020).
58. S. A. King, L. J. Spieß, P. Micke, A. Wilzewski, T. Leopold, E. Benkler, R. Lange, N. Huntemann, A. Surzhykov, V. A. Yerokhin, J. R. C. López-Urrutia, P. O. Schmidt, An optical atomic clock based on a highly charged ion. *Nature* **611**, 43–47 (2022).
59. M. S. Safronova, D. Budker, D. DeMille, D. F. J. Kimball, A. Derevianko, C. W. Clark, Search for new physics with atoms and molecules. *Rev. Mod. Phys.* **90**, 025008 (2018).
60. D. Budker, P. W. Graham, H. Ramani, F. Schmidt-Kaler, C. Smorra, S. Ulmer, Millicharged dark matter detection with ion traps. *PRX Quantum* **3**, 010330 (2022).
61. B. C. Nichol, R. Srinivas, D. P. Nadlinger, P. Drmota, D. Main, G. Araneda, C. J. Ballance, D. M. Lucas, An elementary quantum network of entangled optical atomic clocks. *Nature* **609**, 689–694 (2022).
62. A. J. Brady, C. Gao, R. Harnik, Z. Liu, Z. Zhang, Q. Zhuang, Entangled sensor-networks for dark-matter searches. *PRX Quantum* **3**, 030333 (2022).
63. D. Wineland, C. Monroe, W. Itano, D. Leibfried, B. King, D. Meekhof, Experimental issues in coherent quantum-state manipulation of trapped atomic ions. *J. Res. Natl. Inst. Stan.* **103**, 259–328 (1998).
64. H. Ball, M. J. Biercuk, A. R. R. Carvalho, J. Chen, M. Hush, L. A. De Castro, L. Li, P. J. Liebermann, H. J. Slatyer, C. Edmunds, V. Frey, C. Hempel, A. Milne, Software tools for quantum control: Improving quantum computer performance through noise and error suppression. *Quant. Sci. Tech.* **6**, 044011 (2021).
65. Q-CTRL, Boulder Opal (2023), https://q-ctrl.com/boulder-opal [Online].
66. A. Milne, Construction of a linear ion trap and engineering controlled spin-motional interactions, thesis, University of Sydney (2021).
67. A. Serafini, *Quantum Continuous Variables: A Primer of Theoretical Methods* (CRC Press, 2023), p. 362, 10.1201/9781003250975.
68. Square-lattice GKP code, in *The Error Correction Zoo*, V. V. Albert, P. Faist, Eds. (2022), https://errorcorrectionzoo.org/c/gkp.
69. G. Pantaleoni, B. Q. Baragiola, N. C. Menicucci, Modular bosonic subsystem codes. *Phys. Rev. Lett.* **125**, 040501 (2020).
70. A. J. Brady, A. Eickbusch, S. Singh, J. Wu, Q. Zhuang, Advances in bosonic quantum error correction with Gottesman-Kitaev-Preskill Codes: Theory, engineering and applications. *Prog. Quantum Electron.* **93**, 100496 (2024).
71. K. Fukui, A. Tomita, A. Okamoto, K. Fujii, High-threshold fault-tolerant quantum computation with analog quantum error correction. *Phys. Rev. X* **8**, 021054 (2018).
72. J. E. Bourassa, R. N. Alexander, M. Vasmer, A. Patil, I. Tzitrin, T. Matsuura, D. Su, B. Q. Baragiola, S. Guha, G. Dauphinais, K. K. Sabapathy, N. C. Menicucci, I. Dhand, Blueprint for a scalable photonic fault-tolerant quantum computer. *Quantum* **5**, 392 (2021).
73. K. Noh, C. Chamberland, F. G. Brandão, Low-overhead fault-tolerant quantum error correction with the surface-GKP code. *PRX Quantum* **3**, 010315 (2022).
74. B. W. Walshe, B. Q. Baragiola, H. Ferretti, J. Gefaell, M. Vasmer, R. Weil, T. Matsuura, T. Jaeken, G. Pantaleoni, Z. Han, T. Hillmann, N. C. Menicucci, I. Tzitrin, R. N. Alexander,

Linear-optical quantum computation with arbitrary error-correcting codes. arXiv:2408.04126 [quant-ph] (2024).
75. K. Fukui, R. N. Alexander, P. van Loock, All-optical long-distance quantum communication with Gottesman-Kitaev-Preskill qubits. *Phys. Rev. Res.* **3**, 033118 (2021).
76. O. Hahn, G. Ferrini, R. Takagi, Bridging magic and non-Gaussian resources via Gottesman-Kitaev-Preskill encoding. arXiv:2406.06418 [quant-ph] (2024).
77. J. Conrad, The fabulous world of GKP codes. arXiv:2412.02442 [quant-ph] (2024).
78. B. W. Walshe, B. Q. Baragiola, R. N. Alexander, N. C. Menicucci, Continuous-variable gate teleportation and bosonic-code error correction. *Phys. Rev. A* **102**, 062411 (2020).
79. B. Royer, S. Singh, S. Girvin, Encoding qubits in multimode grid states. *PRX Quantum* **3**, 010335 (2022).
80. T. Matsuura, H. Yamasaki, M. Koashi, Equivalence of approximate Gottesman-Kitaev-Preskill codes. *Phys. Rev. A* **102**, 032408 (2020).
81. C. Flühmann, J. Home, Direct characteristic-function tomography of quantum states of the trapped-ion motional oscillator. *Phys. Rev. Lett.* **125**, 043602 (2020).
82. S. Ahmed, Quantum state tomography with conditional generative adversarial networks, https://github.com/quantshah/qst-cgan (2021).
83. S. Ahmed, C. Sánchez Muñoz, F. Nori, A. F. Kockum, Quantum state tomography with conditional generative adversarial networks. *Phys. Rev. Lett.* **127**, 140502 (2021).
84. I. Strandberg, Simple, reliable, and noise-resilient continuous-variable quantum state tomography with convex optimization. *Phys. Rev. App.* **18**, 044041 (2022).
85. V. V. Albert, Bosonic coding: Introduction and use cases. arXiv:2211.05714 [quant-ph] (2022).
86. Y. Xu, Y. Wang, V. V. Albert, Multimode rotation-symmetric bosonic codes from homological rotor codes. *Phys. Rev. A* **110**, 022402 (2024).
87. P. Carruthers, M. M. Nieto, Phase and angle variables in quantum mechanics. *Rev. Mod. Phys.* **40**, 411–440 (1968).
88. G. Summy, D. Pegg, Phase optimized quantum states of light. *Opt. Commun.* **77**, 75–79 (1990).
89. K. K. Sabapathy, C. Weedbrook, ON states as resource units for universal quantum computation with photonic architectures. *Phys. Rev. A* **97**, 062315 (2018).
90. R. T. Sutherland, R. Srinivas, Universal hybrid quantum computing in trapped ions. *Phys. Rev. A* **104**, 032609 (2021).
91. F. Wolf, C. Shi, J. C. Heip, M. Gessner, L. Pezzè, A. Smerzi, M. Schulte, K. Hammerer, P. O. Schmidt, Motional Fock states for quantum-enhanced amplitude and phase measurements with trapped ions. *Nat. Commun.* **10**, 2929 (2019).
92. H. Cramér, *Mathematical Methods of Statistics* (*PMS-9*) (Princeton Univ. Press, 1946), doi:10.1515/9781400883868.
93. C. R. Rao, Information and the accuracy attainable in the estimation of statistical parameters. *Bull. Calcutta Math. Soc.* **37**, 81–91 (1945).
94. M. G. Paris, Quantum estimation for quantum technology. *Int. J. Quant. Inf.* **07**, 125–137 (2009).
95. J. S. Sidhu, P. Kok, Geometric perspective on quantum parameter estimation. *AVS Quant. Sci.* **2**, 014701 (2020).
96. A. Y. Kitaev, Quantum measurements and the Abelian stabilizer problem. arXiv:quant-ph/9511026 (1995).
97. J. Shapiro, S. Wagner, Phase and amplitude uncertainties in heterodyne detection. *IEEE J. Quantum Electron.* **20**, 803–813 (1984).
98. R. Shaniv, R. Ozeri, Quantum lock-in force sensing using optical clock Doppler velocimetry. *Nat. Commun.* **8**, 14157 (2017).
99. F. Bonus, C. Knapp, C. H. Valahu, M. Mironiuc, S. Weidt, W. K. Hensinger, Ultrasensitive single-ion electrometry in a magnetic field gradient. *Nat. Phys.* **21**, 1189–1195 (2024).
100. M. J. Biercuk, H. Uys, J. W. Britton, A. P. VanDevender, J. J. Bollinger, Ultrasensitive detection of force and displacement using trapped ions. *Nat. Nanotechnol.* **5**, 646–650 (2010).

Acknowledgments: We thank H. Wiseman, B. Terhal, and R. Blatt for fruitful discussions. **Funding:** This work was supported by the US Office of Naval Research Global (N62909-24-1-2083), the US Army Research Office Laboratory for Physical Sciences (W911NF-21-1-0003), the US Air Force Office of Scientific Research (FA2386-23-1-4062), the Australian Research Council (FT220100359, FT230100571, DE230100144, CE170100009, and CE170100012), Lockheed Martin, EPSRC Quantum Engineering Centre for Doctoral Training EP/S023607/1 and European Commission PEQEM ERC-2018-STG803665, the Sydney Quantum Academy, the University of Sydney Postgraduate Award scholarship, the Australian Research Council, and H. and A. Harley. **Author contributions:** C.H.V., B.Q.B., and T.R.T. conceived the idea. C.H.V. developed the experimental protocols, performed the experiment, and analyzed the data. M.P.S., B.Q.B., and Z.H. developed theory for the probability distributions, and Z.H. provided theory support for adaptive phase estimation. V.G.M., C.H.V., M.J.M., and T.R.T. contributed to the experimental apparatus, and B.Q.B., M.P.S., Z.H., T.C., N.C.M., and J.C. provided theoretical support. T.R.T. supervised the project. C.H.V., T.R.T., B.Q.B., Z.H., and N.C.M. wrote the manuscript. All authors provided suggestions for the experiment, discussed the results, and contributed to the manuscript. **Competing interests:** The authors declare that they have no competing interests. **Data and materials availability:** All data needed to evaluate the conclusions in the paper are present in the paper; the data are also available in an online repository (https://doi.org/10.5281/zenodo.14512033).

Submitted 2 March 2025
Accepted 26 August 2025
Published 24 September 2025
10.1126/sciadv.adw9757

Science Advances

Quantum-enhanced multiparameter sensing in a single mode

Christophe H. Valahu, Matthew P. Stafford, Zixin Huang, Vassili G. Matsos, Maverick J. Millican, Teerawat Chalermpusitarak, Nicolas C. Menicucci, Joshua Combes, Ben Q. Baragiola, and Ting Rei Tan

Sci. Adv. **11** (39), eadw9757. DOI: 10.1126/sciadv.adw9757